International Journal of **QUANTUM CHEMISTRY**

# The Role of Aromaticity on the Building of Nanohybrid Materials Functionalized with Metalated (Au(III), Ag(III), Cu(III)) Extended Porphyrins and Single-Walled Carbon Nanohorns: A Theoretical Study

Jesús Muñiz,*[a] Enrique Sansores,[b] Alfredo Olea,[a] and Edgar Valenzuela[a]

An *ab initio*, systematic study on the aromaticity involving the group of metalated extended porphyrins, termed *meso*-hexakis(pentafluorophenyl)-substituted[26]hexaphyrin(1.1.1.1.1.1) (HP), was performed for the first time. The aromatic behavior of the system shifted to antiaromatic in the [28]HP analogue, due to the presence of hydrogen atoms that break the orbital symmetry. The absorption bands observed in the experiment were assigned to an intraligand charge transfer, where the intrametallic character is also important. The excited states reveal the absorption of visible light and the possibility of electronic transfer to different systems. We propose a system such as single-walled carbon nanohorns (SWCNHs), due to their special electronic properties, and predict a novel nanohybrid material. The evidence of electronic communication between both species is presented in this work. The HP aromaticity and the spatial configuration of the interaction with SWCNHs are also related to the strength of electronic transfer among the systems, making the HP metalated antiaromatic species and their corresponding nanohybrids potential candidates to be used as building blocks in photovoltaic cell materials. © 2012 Wiley Periodicals, Inc.

## Introduction

Extended porphyrins, called hexaphyrins (HPs), are a new class of conjugated pyrrolic macrocycles that has been the subject of intense study due to their optical, electrochemical, and coordination properties uncommon in porphyrins.[1] Another interesting property seen in expanded porphyrins is the aromaticity of the macrocycles, which is determined by the $\pi$ electrons in the conjugated circuit. These complexes have also special annulene chemistry, that is, the number of $\pi$ electrons in the conjugated circuit usually determines the aromaticity of the macrocycle. Expanded porphyrins show interesting properties depending on their structure, such as Möbius aromaticity,[2,3] nonlinear optics,[4,5] multimetal coordination,[6] and splitting reactions,[7] among others. Knowledge of expanded porphyrins has widely grown due to their accessibility.[8] The regular hexapyrrolic macrocycles have the privilege of conformational flexibility, which provides, as a consequence, a great variety of metal complexes with unique molecular structures and electronic states.[9]

The system under study is a representative of this group, namely the *meso*-hexakis(pentafluorophenyl)-substituted [26]HP(1.1.1.1.1.1) **1** (Chart 1) and the derivatives obtained by Au(III), Ag(III), and Cu(III) metalation of the [26]HP.[10] The system synthesized by Mori and Osuka[10] has a planar and rectangular shape with an aromatic character and a $26\pi$ conjugated circuit. The square planar geometry of the internal nitrogen and two $\beta$-carbon atoms of the inverted pyrroles give it the property of an effective acceptor of metals inside the cycle, as shown by Mori and Osuka.[10] Such metalation was performed with Au(III), Cu(III), and Ag(III) cations. The aromatic behavior reported in this

group of extended porphyrins was dramatically altered, since an antiaromatic character was observed when the system changed from [26]HP to [28]HP, that is, with the addition of hydrogen atoms at the upper and lower levels of the cycle. This set of compounds present absorption bands located in the visible region, which provides them with the capability of being used as materials in photovoltaic cells. Analogous systems, such as Hückel-aromatic N-confused [26]HPs have been theoretically studied by Toganoh and Furuta[11] using density functional theory (DFT) calculations. In this study, a comparison of the total energies of 754 systems indicated that the most stable conformers depend on the degree of confusion, where ring strain and intermolecular hydrogen bonding would play a critical role. The addition of N-confused pyrrole rings into the HP framework yields smaller energy gaps, keeping nuclear independent chemical shift (NICS) values unchanged.

On the other hand, single-walled carbon nanohorns (SWCNHs) are a type of carbon nanotube, first discovered by Iijima et al.[12,13] in the CO ablation of carbon nanotubes, and

[a] *J. Muñiz, A. Olea, E. Valenzuela*
*Cuerpo Académico de Energía y Sustentabilidad, Universidad Politécnica de Chiapas, Calle Eduardo J. Selvas S/N, Col. Magisterial, Tuxtla Gutiérrez, Chiapas, México, C.P. 29010*
*E-mail: jmuniz@upchiapas.edu.mx*

[b] *E. Sansores*
*Materia condensada y criogenia, Instituto de Investigaciones en Materiales, Universidad Nacional Autónoma de México, Apartado Postal 70-360, México DF 04510, México*
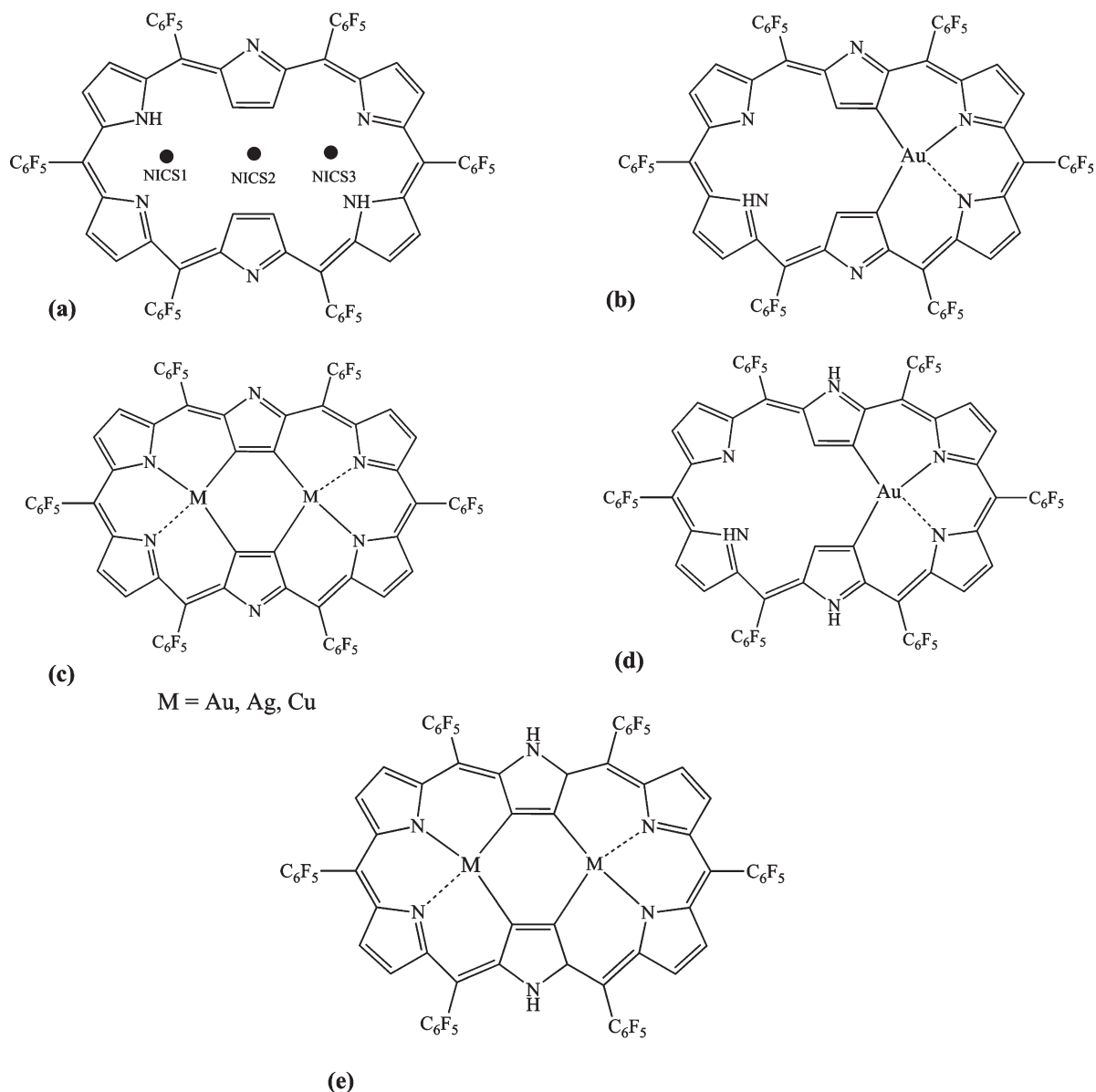
**Chart 1.** a) Molecular structure of the system *meso*-hexakis(pentafluorophenyl)-substituted[26] HP(1.1.1.1.1.1) (**1**); b) Au(III) metalated structure of [26] HP(1.1.1.1.1.1) (**2**); c) M₂(III) metalated structure of [26] HP(1.1.1.1.1.1), with M = Au (compound **3**), M = Ag (compound **6**), M = Cu (Compound **7**); d) Au(III) metalated structure of [28] HP(1.1.1.1.1.1) (**4**); e) Au₂(III) metalated structure of [28] HP(1.1.1.1.1.1) (**5**).

represent an alternative topology of carbonaceous materials. SWCNHs present a conical-shape geometry that gives them special physical and chemical properties that differ from those reported on carbon nanotubes, with a wide range of applications in nanoscience, for example, clean energy technologies as an energy storage device,[14,15] in drug delivery applications,[16] as efficient carriers of adsorbed methane,[17,18] as catalyst supports, and in magnetic resonance analysis, electrochemistry, biosensing applications, photoelectrochemical cells, photodynamic therapy, and photovoltaics, among others. SWCNHs are pure and metal-free, making them harmless to the environment[19] and requiring no purification. SWCNHs paste electrodes have been used for the amperometric determination of concentrated hydrogen peroxide, showing that

SWCNH paste electrodes and edge plane graphite electrodes are interesting alternatives to high surface area platinum electrodes for the determination of concentrated hydrogen peroxide.[20] SWCNHs have also been used as a fluorescent sensing platform to detect nucleic acids.[21]

Further, the electronic states of SWCNHs have also been studied[22] by tight-binding calculations. It was shown that the pentagon at the center of the cone is the most favorable location for emitting tunneling electrons in the presence of an external field. This indicates that SWCNH assemblies might be used as highly localized sources of electrons for tin-plating at a small lithographic scale. Calculations performed by DFT/B3LYP,[23] the semiempirical Austin model AM1[24] and the our own n-layered integrated molecular orbital and molecular

mechanics[25–27] methods show that greater binding energy and reactivity of SWCNH is associated with carbon atoms located near the conical tip of the SWCNH.[28] The tip of a SWCNH is a conic carbon cluster that corresponds to a structure with 5-fold symmetry formed from a two-dimensional graphene sheet due to a 19° inclination defect. The arrangement of carbon atoms at the apex of a conical SWCN tip is analogous to the fullerene hemisphere at the end of an encapsulated carbon nanotube.[29] The latter topological model has been used in the present work to build a full 114 C-atom SWCNH model.

Recently, it was found that SWCNHs are excellent candidates to be used as novel materials in renewable energy applications.[30] It has been shown that electron transfer is present between a SWCNH and the porphyrin a-5-(2-aminophenyl)-a-15(2nitrophenyl)-10,20-bis(2,4,6-trimethylphenyl)-porphyrin ($H_2P$). The evidence of electron and energy transfer is accomplished from the $H_2P$ system to the SWCNH. It has also been shown that electron transfer from a porphyrin system, namely 5,10,15,20-tetrakis(2,4,6-trimethylphenyl)-6′-carboxylquinoxalino[2,3-b′]quinoxalino[12,13-b′]porphyrinatozinc(II) (ZnPBQ) to the conduction band of a $TiO_2$ surface is yielded.[31]

These results position porphyrin systems as potential candidates to be used as materials for solar cells. In this respect, solar energy is an alternative to fossil or nuclear energy supplies, and will play an important role in safety and sustainability by covering rising energy demands in the near future.[32,33] The current cost of electricity from commercial silicon-based solar cells is 10 times higher than that of utility-scale power generation.[34] The traditional inorganic photovoltaic materials present complicated and energy-intensive manufacturing processes, leading expensive production costs. On the other hand, they contain hazardous elements and the devices are heavy, bulky, rigid, and fragile. As a consequence, carbon-based solar cells have emerged as an alternative to this commercial technology.[35,36]

In particular, organic photovoltaics (OPV) belong to this group, comprising crystalline small molecule approaches,[37–39] certain dye-sensitized Grëtel cells,[40] and amorphous polymers (plastics).[41] OPVs are of great relevance due to their promising low cost and high-volume production.[42] Furthermore, OPVs are lightweight[43] and can also take virtually any shape.[44] All these features make OPVs excellent candidates for harvesting solar energy.[45] As a consequence, the Equinox Summit International Committee has suggested the use of OPVs for the basic electrification of 2.5 billion people in rural areas without access to the power grid. Taking the latter into account, the search for new organic photovoltaic materials is an important issue to be addressed.

We propose the systems under study in this work as a potential candidate to be used in OPV applications. The use of metalized extended porphyrins with SWCNHs in applications of electron transfer has not been achieved so far, and no theoretical studies are available on the electronic structure of such nanohybrid materials. The aim of this work is to theoretically understand the aromaticity of metalated extended porphyrins and the electron transfer mechanisms behind the interaction with SWCNHs. The results of this study may aid in the design new nanohybrid materials to be used in clean-energy applications.

## Computational Methods

Full geometry optimizations were performed with DFT at the B3LYP[23] level for the extended porphyrins and SWCNH model. The B3LYP functional combines the exact Hartree–Fock exchange with the Lee, Yang, and Parr correlation functional that includes the most important correlation effects. The Stuttgart small core pseudorelativistic effective core potentials (ECPs)[46] with 19 valence electrons were employed for Au, Ag and Cu. The ECPs were used with the valence triple-f plus one polarization type; that is, the basis set TZVP, which is an optimized contracted Gaussian basis set for Au, Ag, and Cu, calculated with the same methodology as those of the basis computed by Schäfer et al.[47] For the nonmetallic atoms, the 6-31G++(2d2f,p) basis set was used.[48,49] To study the energy interactions among extended porphyrins and a SWCNH, basis set superposition error calculations were performed in accordance with the counterpoise methodology developed by Boys and Bernardi[50] using a density functional that includes dispersion effects, the B97D Grimme's functional,[51] based on Becke's power series ansatz[52] and parameterized by including damped atom-pairwise dispersion corrections of the form $C_6 \cdot R^{-6}$, where $C_6$ are the consistent atomic parameters and $R$ the intermolecular distance. The interaction energy was calculated according to Eq. (1):

$$V(R) = E_{AB}^{AB}(R) - E_{A}^{AB}(R) - E_{B}^{AB}(R) \tag{1}$$

where the lower index refers to the system considered, while the upper index refers to the basis set used. System A refers to the set of HPs under study, while B corresponds to the SWCNH. The excited state calculations were performed using the time-dependent DFT computational methodology (TD-DFT),[53] at the M06-HF level,[54] since B3LYP has failed to describe charge transfer interactions.[55] To model the compounds in solution, TD-DFT calculations were carried out with the isodensity Tomasi's polarized continuous model[56] in $CH_2Cl_2$. Orbital populations were obtained according to the NBO method.[57] The aromaticity calculations were performed according to the NICS methodology developed by Schleyer et al.,[58] where a "ghost" atom is located about the aromatic cycle to quantify the magnetic shielding coming from the diatropic currents 3 produced in the system. All computations were carried out using the GAUSSIAN09 code.[59]

## Results and Discussion

### Structural description

Compound **1** and its derivatives were fully optimized by the method described in the Computational Details section. All optimized structures are shown in Figure 1. After geometry optimization, compound **1** presents a planar geometry with slight deviations near the center of the ring. The spatial representation
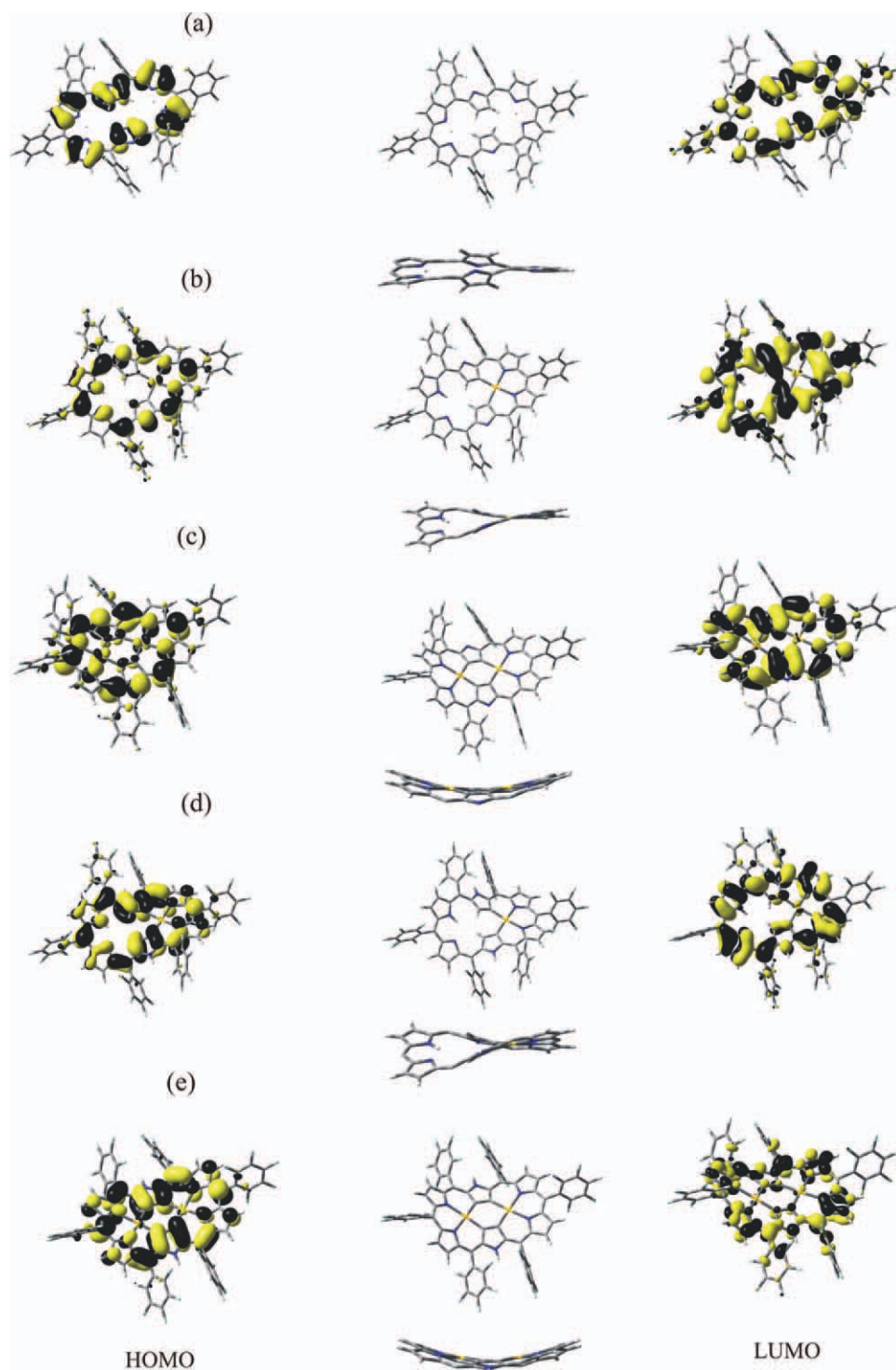
**Figure 1.** Optimized molecular structures of the systems under study: a)–e) represent complexes **1–5**, respectively. The lateral views depict the spatial representation of the frontier MOs HOMO and LUMO. [Color figure can be viewed in the online issue, which is available at wileyonlinelibrary.com.]

twisted structure with a slight deviation from the plane, as can be seen from the view perspective in Figure 1b (the pentafluorophenyl substituents are omitted for clarity in this configuration). The HOMO for this complex has a similar contribution to that of compound **1** and, in this case, a contribution from the Au p orbitals is also present. The contribution from the LUMO is similar to that of compound **1**. The twisted structure reported in system **2** may be attributed to the strength of the Au—C bonds (∼200 pm), which considerably comprises half of the ring and deviates it from the plane. This can also be corroborated from the frontier MOs depicted in Figure 1b, denoting a large amount of charge located in the region of Au—C bonding.

The presence of a second Au atom in complex **3** changes the geometry of the molecule from a twisted to a bent structure, as can be observed from the lateral view in Figure 1c, which is in clear agreement with the results found by experiment.[10] In this complex, the Au p orbitals contribute to the HOMO, while for the LUMO, the contributions are located on the N atoms. A comparison of the structural parameters found experimentally and by the present theoretical method is reported in Table 1, where bond distances and angles are included. The same behavior observed in complex **2** is present in complex **3**, that is, a large amount of orbital population is allocated around the metal centers (as observed from the frontier MOs), providing as a consequence a bend along the plane of the HP.

Geometry optimizations of complexes **4** and **5**, the metalated derivatives of complexes **2** and **3**, respectively, were also carried out. The theoretical results for these compounds are in reasonable agreement with those found by experiment, as can be seen from Table 1. The HOMO of complex **4** is mainly located at the center of the ring, as can be seen from Figure 1d, while the LUMO is mainly located on the C atoms around the ring. Complex **5** shows a similar pattern on the frontier MOs to that of

of the frontier molecular orbitals (MOs) is also shown in Figure 1a; the highest occupied molecular orbital (HOMO) is composed of π-orbitals located on the C and N atoms at the ring. The lowest unoccupied molecular orbital (LUMO) has a contribution of π-orbitals on the center of the ring. Complex **2**, which has an Au atom located close to the center of the molecule, presents a

**Table 1.** Structural parameters of the complexes under study.

| Bond | Experimental (Å) | Theory (Å) | Bond angle | Angle (deg.) experiment | Angle (deg.) theory |
|---|---|---|---|---|---|
| Bond lengths and angles for complex **1** | | | | | |
| N1—C5 | 1.37 | 1.42 | C7—N3—C8 | 105.23 | 104.06 |
| N2—C9 | 1.38 | 1.42 | C9—C15—N6 | 127.00 | 130.09 |
| C5—C6 | 1.41 | 1.43 | C11—N4—C12 | 107.74 | 104.19 |
| C9—C10 | 1.38 | 1.43 | C12—C13—C14 | 127.46 | 129.58 |
| N3—C7 | 1.38 | 1.40 | C13—C14—N5 | 126.65 | 130.28 |
| Bond lengths and angles for complex **2** | | | | | |
| Au1—C1 | 1.98 | 2.03 | C1—Au1—C2 | 91.44 | 91.82 |
| Au1—C2 | 2.01 | 2.03 | N1—Au1—N2 | 88.88 | 88.67 |
| Au1—N1 | 2.08 | 2.13 | C5—N1—Au1 | 126.72 | 126.11 |
| Au1—N2 | 2.08 | 2.13 | C7—C2—Au1 | 124.16 | 122.82 |
| N1—C5 | 1.37 | 1.38 | N2—Au1—C1 | 90.73 | 90.37 |
| Bond lengths and angles for complex **3** | | | | | |
| Au1—Au2 | 4.22 | 4.21 | C1—Au1—C2 | 88.57 | 89.74 |
| Au2—C3 | 2.04 | 2.03 | N1—Au1—N2 | 86.54 | 86.30 |
| Au2—C4 | 2.02 | 2.03 | C3—Au2—C4 | 88.98 | 89.74 |
| Au2—N5 | 2.11 | 2.14 | N6—Au2—N5 | 87.02 | 86.30 |
| Au2—N6 | 2.10 | 2.14 | C5—N1—Au1 | 126.28 | 125.58 |
| Bond lengths and angles for complex **4** | | | | | |
| Au1—C1 | 1.98 | 2.02 | C1—Au1—C2 | 91.44 | 91.98 |
| Au1—C2 | 2.01 | 2.02 | N1—Au1—N2 | 88.88 | 89.07 |
| Au1—N1 | 2.08 | 2.11 | C5—N1—Au1 | 126.72 | 125.65 |
| Au1—N2 | 2.08 | 2.11 | C7—C2—Au1 | 124.16 | 122.62 |
| N1—C5 | 1.37 | 1.40 | N2—Au1—C1 | 90.73 | 90.40 |
| Bond lengths and angles for complex **5** | | | | | |
| Au1—Au2 | 4.22 | 4.26 | C1—Au1—C2 | 88.57 | 89.48 |
| Au2—C3 | 2.04 | 2.03 | N1—Au1—N2 | 86.54 | 85.92 |
| Au2—C4 | 2.02 | 2.03 | C3—Au2—C4 | 88.98 | 89.48 |
| Au2—N5 | 2.11 | 2.13 | N6—Au2—N5 | 87.02 | 85.92 |
| Au2—N6 | 2.10 | 2.12 | C5—N1—Au1 | 126.28 | 125.32 |
| Bond lengths and angles for complex **6** | | | | | |
| Ag1—Ag1 | – | 4.32 | C1—Ag1—C2 | – | 87.3 |
| Ag1—C3 | – | 2.06 | N1—Ag1—N2 | – | 86.4 |
| Ag1—C4 | – | 2.06 | C3—Ag2—C4 | – | 87.3 |
| Ag1—N5 | – | 2.14 | N6—Ag2—N5 | – | 86.4 |
| Ag1—N6 | – | 2.14 | C5—N1—Ag1 | – | 127.2 |
| Bond lengths and angles for complex **7** | | | | | |
| Cu1—Cu2 | – | 4.20 | C1—Cu1—C2 | – | 81.0 |
| Cu1—C3 | – | 1.94 | N1—Cu1—N2 | – | 89.2 |
| Cu1—C4 | – | 1.94 | C3—Cu2—C4 | – | 81.0 |
| Cu1—N5 | – | 1.98 | N6—Cu2—N5 | – | 89.2 |
| Cu1—N6 | – | 1.97 | C5—N1—Cu1 | – | 126.8 |

**Table 2.** Total electronic energies of the systems under study.

| System | Energy (hartrees) |
|---|---|
| 1 | −5845.2128 |
| 2 | −5978.9981 |
| 3 | −6112.6731 |
| 4 | −5980.2721 |
| 5 | −6113.9477 |
| 6[a] | −6133.1968 |
| 7[b] | −6234.0295 |

[a] Ag2 metallated HP. [b] Cu2 metallated HP.

energy due to the attachment of Au atoms at the extended porphyrin, as reported in Table 2. The structural difference in complexes **4** and **5** is the attachment of the hydrogen atoms to the upper and lower pyrrole groups on the HP. The geometry is essentially the same than those in complexes **2** and **3**, but the shape of the frontier MOs is altered; the interacting $\pi$ orbitals break the symmetry and populate the region of the central pyrroles, while the electronic population on the metallic centers is substantially reduced with only slight contributions coming from the Au $d_{xz}$ orbitals.

### Aromatic character

To understand the aromatic properties of the compounds under study, NICS calculations were performed in complexes **1**–**5**. These results are summarized in Table 3. In compound **1**, the

**Table 3.** NICS values located at different geometrical centers.

| Compound[a] | 1 | 2 | 3 | 4 | 5 | 6 | 7 |
|---|---|---|---|---|---|---|---|
| NICS1 (ppm) | −11.77 | | | | | | |
| NICS2 (ppm) | −14.89 | −12.33 | −10.16 | 18.74 | 34.41 | −9.49 | −8.54 |
| NICS3 (ppm) | −11.97 | −11.94 | | 21.55 | | | |

[a] NICS1 is at the left side of the geometrical center of the ring, NICS2 is at the geometrical center of the ring and NICS3 is at the left side of the center of the ring. See Chart 1a for reference.

ghost atoms were aligned to the center of the ring (see Chart 1 for more details). According to the NICS values, compound **1** appears to be strongly aromatic. In the case of complex **2**, the ghost atoms were located at a region far from the gold atoms and aromatic behavior is also observed. In the case of complex **3**, a ghost atom was located at the center of the ring on the intermediate zone between the gold atoms (Chart 1). As can be seen from Table 3, complex **3** reveals strong aromaticity at this location. Complexes **4** and **5** show strong antiaromaticity that can be inferred from the hydrogen atoms attached to the N atoms on the upper and lower sides of the molecules, that is, the [28]HP configuration. This striking result is in agreement with the experiment performed by Mori and Osuka,[10] where the antiaromatic behavior in porphyrins was reported for the first time. Such character is uncommon in extended porphyrins. The protonation on complexes **4** and **5** alters the distribution of $\pi$ orbitals around the cycle (see the HOMOs depicted in Figs. 1d and 1e), and consequently alters the nature of the existing diatropic currents, giving the system the observed antiaromatic character. The attachment of H atoms at the pyrrole group shifts the nature of the complex from aromatic to antiaromatic. The latter can be understood from the analysis of the frontier MOs depicted in Figure 1: compound **2** presents a $26\pi$ conjugated circuit, observed in the spatial distribution of the HOMO, while at complex **4**, the addition of the H atoms changes the symmetry and yields four bonding $\pi$-orbitals.

The presence of $\pi$ electrons at the center of the ring breaks the circulation of electronic currents caused by the $26\pi$

**4**, as is depicted in Figure 1e. The characteristic planarity observed in complexes **2**–**5** is due to the presence of the gold atoms, as can be inferred from the optimized geometry for compound **1**, where no gold atoms are present. The planarity of the complex is a consequence of the stabilization in the

electrons, and gives rise to the antiaromatic behavior reported with the NMR shielding results, calculated using the NICS methodology. As has already been reported, the metalation of two Au atoms (complex **3**) at the central side of the ring bends the structure of the HP and stabilizes the overall energy. Energy stabilization rectifies the twisting, bringing the molecular structure of the HP to a flat, bent geometry computed with our calculations, in excellent agreement with experiment.[10] The stability in system **3** with respect to **2** is also correlated with the aromatic character, since the NICS value for **3** is larger than that of **2** (Table 3). This is in agreement with the work by Toganoh and Furuta,[11] where a correlation between the relative energies of N-confused HPs and their NICS values was found. As is reported in Table 2, the HP tends to be stabilized when the addition of Au atoms is supplied; consequently, the total energy is also decreased. This is also in accordance with results given by Toganoh and Furuta.[11] A correlation between the number of intramolecular hydrogen bonds (N…H) and the relative energies in N-confused HPs was established. In the present work, system **3** presents two additional Au…H intramolecular hydrogen bonds, providing, as a consequence, stabilization of the overall energy. A minimum occurs in compound **3**, where the NICS values are the greatest among the aromatic Au series of HPs.

In the case of compound **2**, where the metalation of an Au atom is achieved, the overall aromatic behavior is significantly reduced (Table 3). The latter suggests a correlation between the stability of the species and the aromatic character, which is representative of the aromatic compounds[60,61] and is in agreement with the results by Toganoh and Furuta.[11]

The increase in the NICS value in complex **3** might be attributed to the presence of dxz orbitals coming from the Au atoms; that is, the d orbitals supply electrons to the internal electronic currents on the plane of the HP, quantified by magnetic shielding measurements. This behavior has been reported on trinuclear Au(I) atoms and extended systems[11,62] where the d–d interaction plays an important role in aromaticity. The complexes under study maintain a $\pi$-character in the aromaticity, but the presence of a $\delta$-character cannot be neglected.

On the other hand, when Ag and Cu atoms are attached around the center of the cycle, we observe an analogous aromatic character to that of complex **3** (Table 3). That is, HP **6**, metalated with two Ag(III) cations, represents the analogue system **3** and exhibits similar NICS values to those of the dinuclear Au system. The frontier MOs of the analogue Au HP are equivalent to this system (see Fig. 1c for comparison), with the presence of $d_{xz}$ orbitals at the Ag atoms, suggesting the presence of $\delta$-aromaticity reported in system **3**; consequently, the d electrons in the circuit increase the aromatic character and stabilize the energy. The Cu metalated HP (complex **7**) reports an analogous aromaticity to that of complex **2**; the NICS value of this compound is reduced due to the smaller population found for the d-electrons according to the spatial representation of the frontier MOs.

As already stated, a shift in aromaticity is present on the change from [26]HP to [28]HP, when hydrogenation takes place. The natural charges remain virtually unchanged along the aromatic cycles for complexes **2** and **4**, and the attachment of H atoms at the pyrrole groups gives a new configuration to the spatial distribution on the frontier MOs, that is, the presence of bonding $\pi$-orbitals at the geometrical center of the HP and the absence of d-orbitals break the current flow, leading to the antiaromatic character calculated for compound **4**. The same tendency is also reported for HPs **3** and **5**: the current flow is altered in complex **5**, no d-electrons are involved and antiaromaticity is the ruling character.

## Excited states

The absorption bands were modeled in accordance with the TD-DFT methodology. It is known that TD-DFT yields errors for the excitation energies of charge transfer excited states when combined with standard exchange-correlation functionals, such as B3LYP.[23] Besides, the correct $1/R$ asymptotic behavior of charge transfer states with respect to $R$ between the separated charges of the charge transfer state is not reproduced by TD-DFT using such functionals. Many density functionals are unable to treat the polarizability of conjugated systems[63] and thus they fail for the ground-state energy of systems, such as protonated polyenes.[64] This failure may be due to an incorrect long-range behavior of the effective potentials generated by the density functionals widely used because of their accuracy for broad areas of other thermochemical predictions. This incorrect long-range behavior comes from a self-interaction error in local DFT exchange functionals. The breakdown for systems with medium-range electron–electron coupling can be attenuated using an improved functional.[64] Consequently, we used the functional M06-HF,[54] with full Hartree–Fock exchange, eliminating self-exchange interactions at long range. This functional has given good performance in TD-DFT calculations of charge transfer states, and it also satisfies the uniform electron gas limit, giving, on average, better results than the B3LYP functional.[23]

For the systems under study, the absorption band maxima are centered beyond 500 nm with high oscillator strengths, indicating no luminescent character. The absorption profiles computed for complexes **1**–**7** are presented in Table 4, and may be associated with the absorption bands located in the

**Table 4.** Excited state calculation in accordance to TD-DFT methodology.

| System | Multiplicity | Energy (eV) | Wavelength (nm) | Oscillator strength |
|---|---|---|---|---|
| Aromatic compounds | | | | |
| **1** | Singlet | 2.05 | 603.4 (550)[a] | 0.8501 |
| **2** (1 Au atom) | Singlet | 1.98 | 625.8 (610)[a] | 0.2228 |
| **3** (2 Au atoms) | Singlet | 1.97 | 630.1 (680)[a] | 0.4493 |
| **6** (2 Ag atoms) | Singlet | 1.79 | 691.0 | 0.3031 |
| **7** (2 Cu atoms) | Singlet | 1.81 | 683.1 | 0.0918 |
| Antiaromatic compounds | | | | |
| **4** (1 Au atom) | Singlet | 2.19 | 566.7 (500)[a] | 0.0102 |
| **5** (2 Au atoms) | Singlet | 1.96 | 630.8 (530)[a] | 0.0467 |

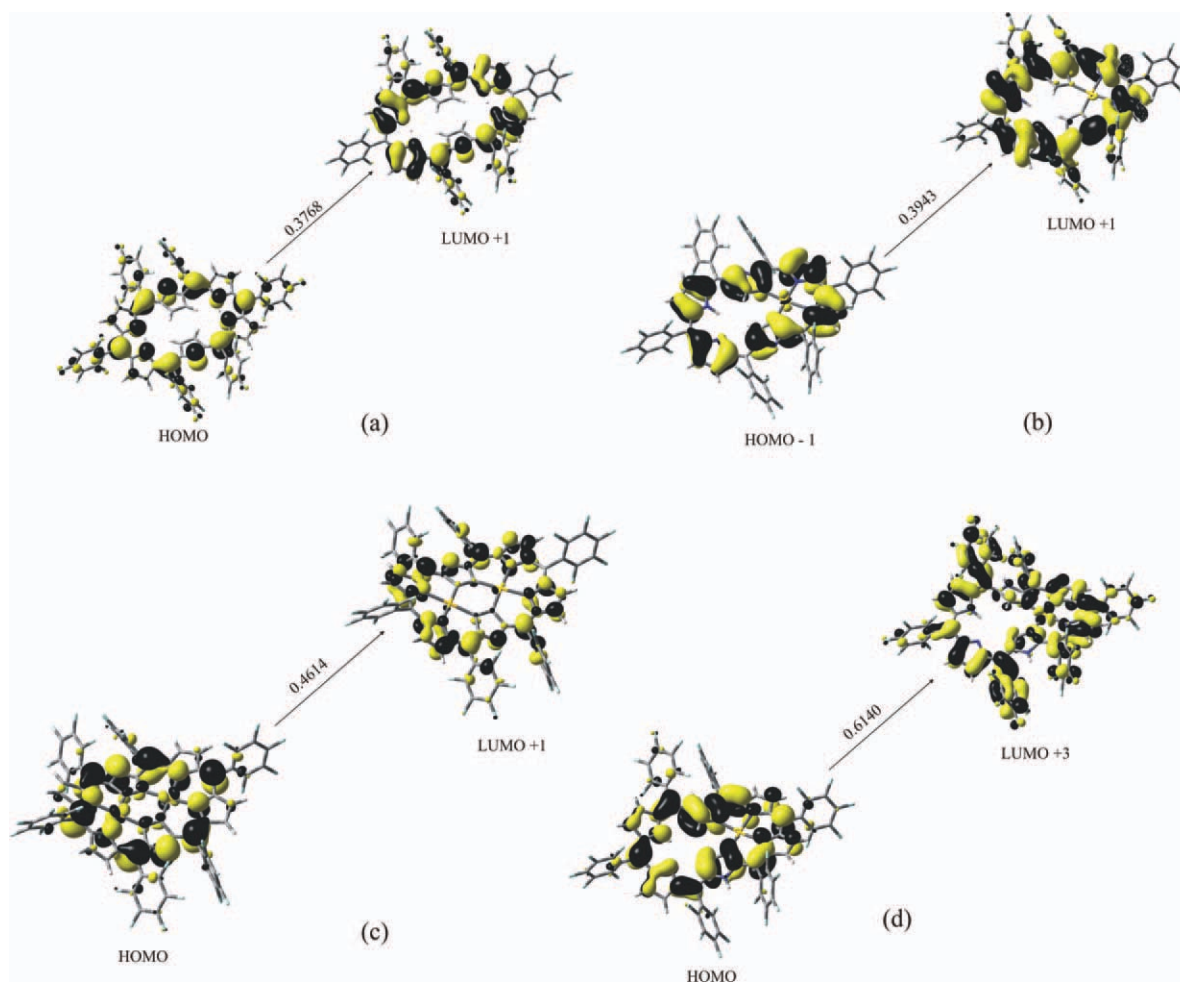[a] Experimental data are given in parenthesis from Ref. [10].

**Figure 2.** Single electron transitions of the absorption bands with the largest |CI—coefficients|. The transitions a)–d) refer to Systems **1**–**4**. [Color figure can be viewed in the online issue, which is available at wileyonlinelibrary.com.]

experiment. The Soret-like behavior found in the experiment is also present in the current series of calculations; that is, the aromatic HPs **1**–**3** and **6** have a high oscillator strength, which may be related to a high molar absorptivity, as was found in Mori's experiment. On the other hand, the antiaromatic HPs **4** and **5** present a low oscillator strength, which may also be assigned to a low molar absorptivity, as is actually reported in experiment (Table 4).

To understand the nature of the excited states involved in the absorption bands, the transitions with the largest CI-coefficients are presented in Figure 2. The most probable set of MOs where a one-electron transition may take place are presented. These results are also summarized in Table 4. The absorption band in compound **1** was located at 603.4 nm and the transition is depicted in Figure 2a, which can be assigned to the 550 nm band observed experimentally. The transition is triggered from the HOMO to the LUMO+1. The spatial representation of the HOMO is composed of $\pi$ orbitals located around the aromatic cycle as depicted in Figure 2a, while the LUMO+1 is a virtual orbital where no electrons reside; nevertheless, it gives a picture of the most probable sites where the electron would be transferred to after it is excited. It was

found that the $\pi$ orbitals were unaltered, indicating that the absorption band originated from a charge transfer around the aromatic cycle of the HP.

Complex **2** presents an experimental absorption band located at 610 nm,[10] which may be assigned to the 625.8 nm band computed with the TD-DFT methodology. The MOs involved in the transition are depicted in Figure 2b. In this case, the electronic transition comes from the HOMO−1 to the LUMO+1. The first MO is mainly composed of $\pi$ orbitals around the cycle with a $d_z^2$ mixture allocated at the Au atom on the periphery of the HP, while at the LUMO+1, no contribution is found on the Au atom. As a consequence, it appears that the electronic transition giving rise to the absorption band found experimentally for complex **2** corresponds to a metal to ligand charge transfer interaction, where the intraligand (IL) character is also important.

Complex **4** represents the antiaromatic analogue of complex **2**. The absorption band was assigned to the one-electron transition located at 567 nm with an oscillator strength of 0.0102, which corresponds to the 500 nm experimental band.[10] As depicted in Figure 2d, the transition with the largest CI coefficient is a higher energy process starting at the HOMO and
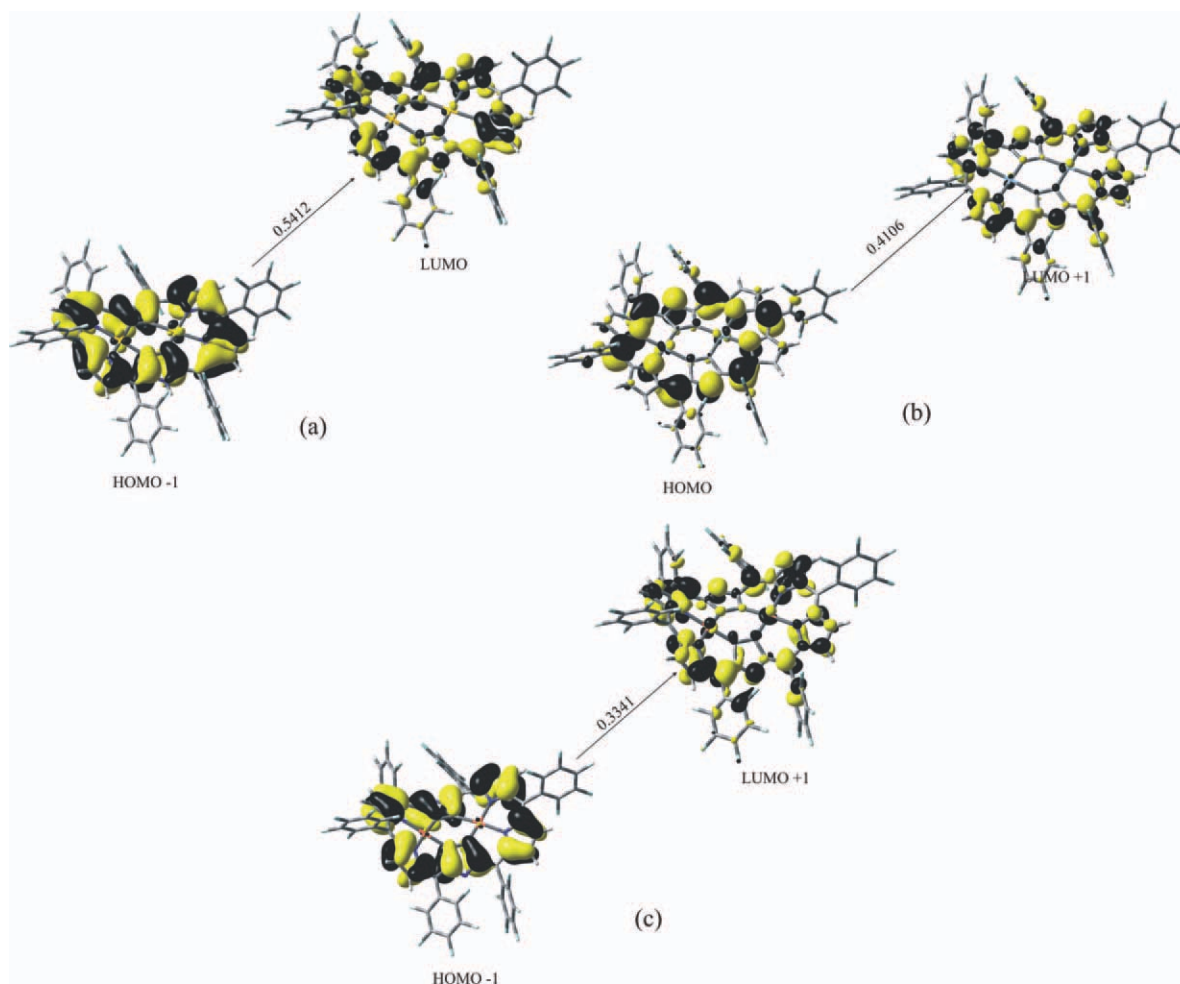
**Figure 3.** Single electron transitions of the absorption bands with the largest |CI—coefficients|. The transitions a)–c) refer to Systems **5**–**7**. [Color figure can be viewed in the online issue, which is available at wileyonlinelibrary.com.]

going to the LUMO+3. The $\pi$ orbitals involved in this process are allocated to the HP cyclic ring. Nevertheless, the absorption mechanism in this case appears to be ruled by a charge transfer from the $\pi$ orbitals of the aromatic ring at the HOMO to the Au $d_{xz}$ orbital of the LUMO+3, with the characteristic IL character reported in the analogue complex **2**, which is also extended to the pentafluorophenyl substituents attached to the cycle.

Complex **3** presents an absorption band observed experimentally at 680 nm, which can be associated with the computed transition at 630 nm (Fig. 1c), with an oscillator strength of 0.449. According to the excitation (HOMO $\rightarrow$ LUMO+1), the d-aromatic character of the HP is mainly responsible for the electron transfer, that is, the electronic charge allocated on the $d_{xz}$ orbitals at the Au atoms on the HOMO are triggered to the same Au $d_{xz}$ on the LUMO+3, while the contribution from the $\pi$ orbitals cannot be neglected. As a consequence, the transition involved may be addressed to a metal centered charge transfer.

The metalated Au$_2$ antiaromatic analogue is presented in Figure 3a. The absorption band calculated for this excitation is located at 631 nm, presenting a shift with regard to the experimental band of about 100 nm. It may be due to the small

molar absorptivity $\varepsilon$ ($\sim 10^5$ M$^{-1}$ cm$^{-1}$), which is 150% smaller than those excitations with the largest $\varepsilon$ coefficients. The oscillator strength of this interaction is very small (0.0102) as well, in accordance with the reported experimental value. As depicted in Figure 3a, it was found that the transition is mainly ruled by an IL charge transfer from the hybrid sp orbitals allocated to the HP pyrrole groups to the $\pi$ orbitals on the same ligands. A slight contribution from the HOMO–1 Au $d_{xz}$ orbitals to the Au $d_{xz}$ on the LUMO is also present, that is, the intrametallic character of the interaction in this system is relevant only to a small extent.

The absorption band of the metalized Ag$_2$ HP has not been obtained experimentally. In this study, we predict the electronic nature for the interactions involved in the possible absorption band: the interaction with the greatest oscillator strength is a low-lying transition located at 690 nm. The transition comes from the HOMO to the LUMO+1. The $\pi$–$\pi^*$ interaction has an analogue character to that of the Au species, and the intrametallic $d_{xz}$–$\pi^*$ character also has an important contribution on the absorption band (Fig. 3b).

The low-energy absorption band calculated for the aromatic metalated Cu$_2$ HP is centered at 683 nm. In this case, a $\pi$–$\pi^*$
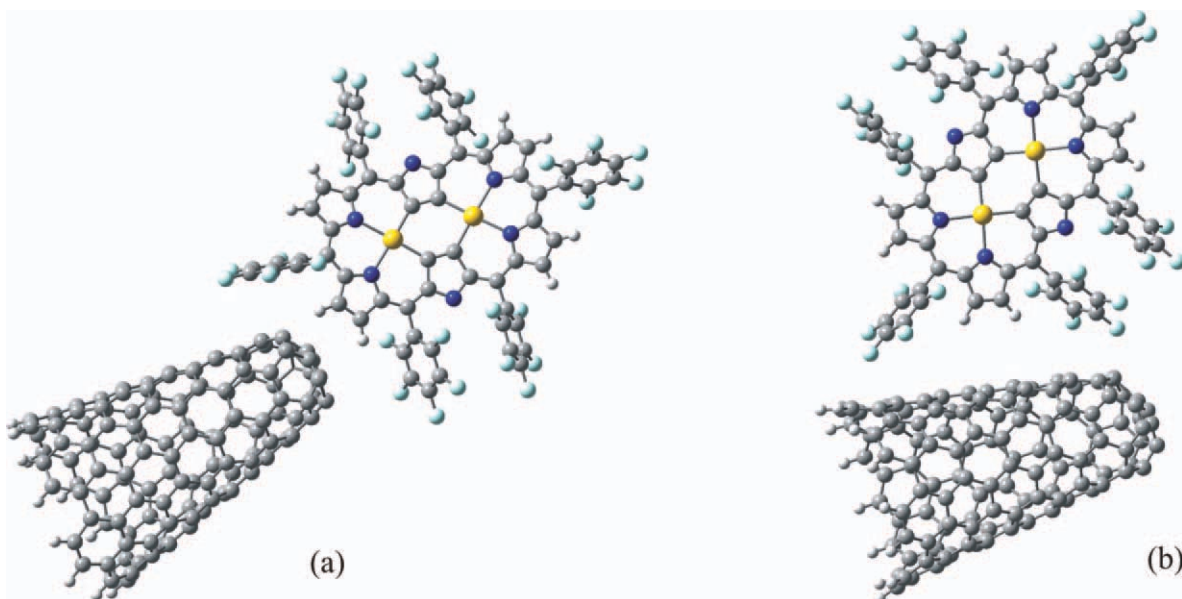
**Figure 4.** Molecular representation of the model systems used to study the intermolecular interactions among SWCNHs and HPs species: a) face-to-face arrangement; b) lateral wall interaction. [Color figure can be viewed in the online issue, which is available at wileyonlinelibrary.com.]

transition was found coming from the HOMO-1 to the LUMO+1. Nevertheless, as depicted in Figure 3c, a ligand to metal charge transfer contribution is also present.

### HPs and SWCNH intermolecular interactions

The available properties of electronic communication among the group of HPs and a SWCNH were also studied. To correlate the interaction energies with the capabilities of electron transfer between the SWCNH and the HP, two basic molecular models were suggested. The potential energy surface was scanned according to Eq. (1) to find an interaction between the extended porphyrin and the SWCNH. In the first model, depicted in Figure 4a, both systems interact through the tip of the SWCNH and one of the pyrrole groups at the HP. This site was chosen as a weaker steric repulsion would be found, due

to the small electronic population found at the frontier MOs (Fig. 1). In the second model, the HP is set adjacent to the SWCNH wall, as presented in Figure 4b. The distances considered in the interaction were taken from a small distance (~300 pm) to larger distances, where the presence of electronic communication would be virtually absent (>600 pm).

The interaction energy curve representing the face-to-face arrangement of system **1** and the SWCNH is shown in Figure 5. A fully repulsive interaction was observed. At short distances, no binding is reported, and at longer distances, the interaction between the two units is completely lost. In the second arrangement (Fig. 6), where the HP interacts with the SWCNH wall, the opposite behavior was observed, that is, at short distances, a high energy is obtained, while for large distances the energy remains constant. A shallow minimum is observed, located at about 410 nm.
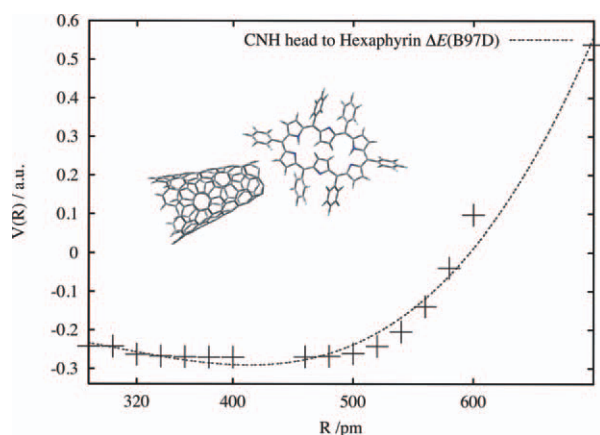


**Figure 5.** Potential energy curve $V(R)$ for the face-to-face arrangement: Compound **1** + SWCNH nanohybrid system. [Color figure can be viewed in the online issue, which is available at wileyonlinelibrary.com.]
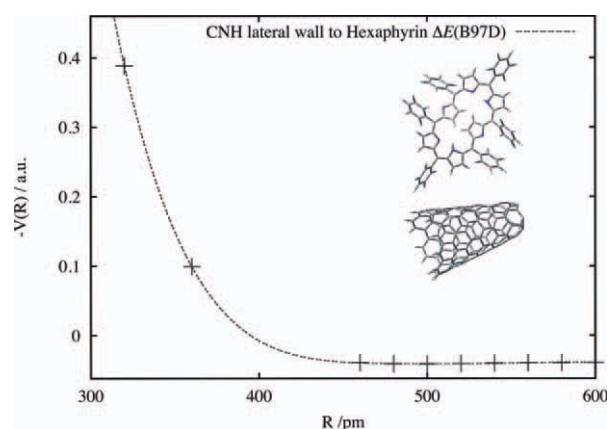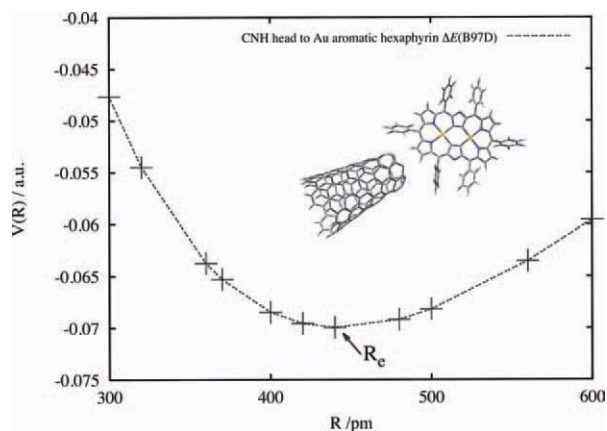


**Figure 6.** Potential energy curve $V(R)$ for the lateral arrangement: Compound **1** + SWCNH nanohybrid system. [Color figure can be viewed in the online issue, which is available at wileyonlinelibrary.com.]

**Figure 7.** Potential energy curve $V(R)$ for the face-to-face arrangement: complex **3** + SWCNH nanohybrid system. [Color figure can be viewed in the online issue, which is available at wileyonlinelibrary.com.]



**Figure 9.** Potential energy curve $V(R)$ for the face-to-face arrangement: complex **5** + SWCNH nanohybrid system. [Color figure can be viewed in the online issue, which is available at wileyonlinelibrary.com.]

The aromatic $Au_2$ HP (system **3**) was also studied at the two geometrical arrangements described above. In the face-to-face arrangement, a clear minimum was found located at 430 nm, indicating that an intermolecular interaction is present between the metalated HP and the SWCNH, as is presented in Figure 7. This result reveals that the presence of the Au atoms at the aromatic cycle is responsible for the weak chemical bonding. As no ligand has been considered in this model, the bonding may be assigned to dispersive interactions described in an approximate fashion by the B97D Grimmes' functional.[50] The interaction from the HP at the SWCNH walls has also been characterized by potential energy scanning, and the calculations are summarized in Figure 8: a shallow minimum is also found, but a repulsive nature at long distances rules the nature of the interaction.

The $Au_2$ antiaromatic HP (system **5**) was also studied with the model. A minimum in the face-to-face configuration was found and presented in Figure 9, the equilibrium energy is slightly increased and the bonding distance is decreased to 350 pm, yielding a strong interaction between the HP and the SWCNH. The ionic nature of the attraction might be another mechanism behind the interaction, as no ligand is considered
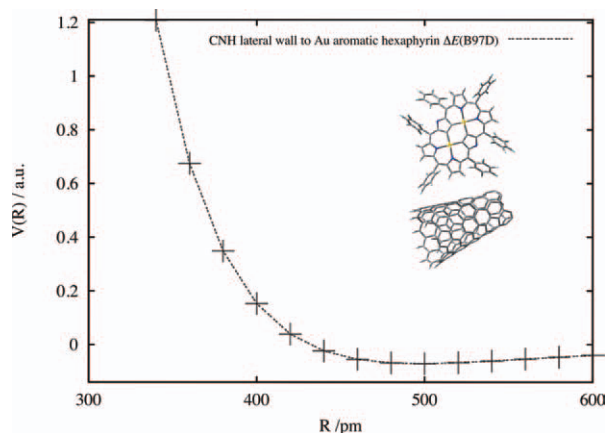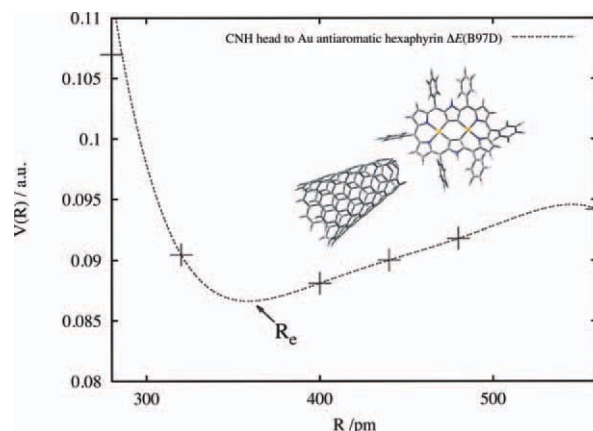
to bridge both systems. Besides, the new aromatic and antiaromatic character coming from the presence of the Au atoms at the cycle of the HP modifies the electronic structure of the system with respect to the first case.

The weak attraction may be understood from the electronic charge distributed at the equilibrium geometry reported in the corresponding graphs. An NBO calculation was performed (Table 5) at those geometries and a

**Table 5.** NBO partial charges on the nanohybrid system CHN + extended porphyrin. All systems refer to the face-to-face arrangement.

| System | CNH | Extended porphyrin |
|---|---|---|
| CNH + HP(**3**) | −0.00253 | 0.00253 |
| CNH + HP(**5**) | −0.00974 | 0.00974 |
| CNH + HP(**7**) | −0.01012 | 0.01012 |
| HP stands for Hexaphyrin. | | |

$[SWCNH]^-[HP]^+$ configuration was found for both the $Au_2$ aromatic and antiaromatic species. Consequently, the bonding found by the interaction energies analysis also presents an
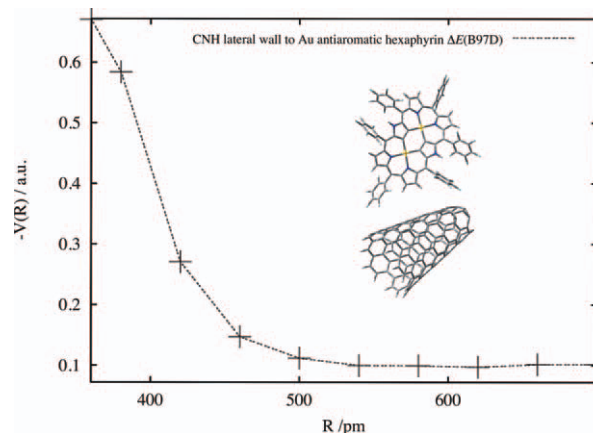


**Figure 8.** Potential energy curve $V(R)$ for the lateral arrangement: complex **3** + SWCNH nanohybrid system. [Color figure can be viewed in the online issue, which is available at wileyonlinelibrary.com.]
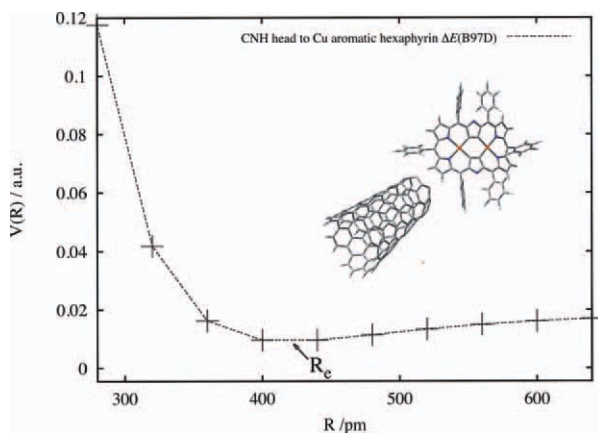


**Figure 10.** Potential energy curve $V(R)$ for the lateral arrangement: complex **5** + SWCNH nanohybrid system. [Color figure can be viewed in the online issue, which is available at wileyonlinelibrary.com.]
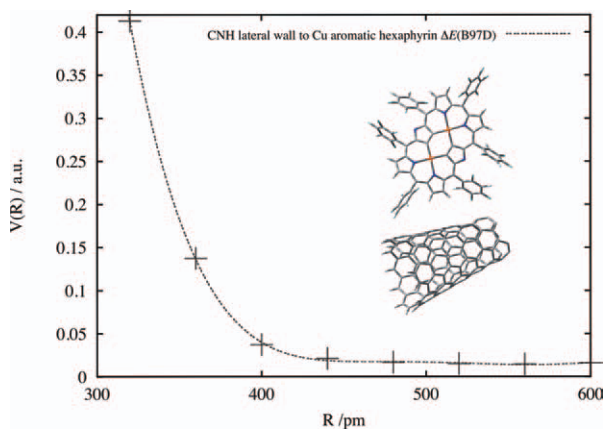
**Figure 11.** Potential energy curve $V(R)$ for the face-to-face arrangement: complex **7** + SWCNH nanohybrid system. [Color figure can be viewed in the online issue, which is available at wileyonlinelibrary.com.]



**Figure 12.** Potential energy curve $V(R)$ for the lateral arrangement: complex **7** + SWCNH nanohybrid system. [Color figure can be viewed in the online issue, which is available at wileyonlinelibrary.com.]

ionic nature. Furthermore, the presence of a ligand connecting the HP and the SWCNH would only increase the attraction, but the possibility of electronic communication among

these species would mainly be ruled by the electrostatic contribution.

The interaction of system **5** with the SWCNH lateral walls is reported in Figure 10, and a merely repulsive interaction was found for this arrangement. The latter is consistent with previous results,[65] where attraction is virtually absent at the tip of the HP.

The same analysis was also applied to the aromatic $Cu_2$ complex (system **7**) to compare the behavior shown for the Au HP analogues. As shown in Figure 11, an equilibrium configuration was located at about 425 nm ($R_e$) in the face-to-face configuration. At short distances, large repulsion energy was clearly identified, which may be due to the large steric repulsion. At long distances, the interaction is virtually lost, as would be expected from the behavior observed in the complexes under study.

The interaction between the SWCNH walls and the HP presents a clear repulsive character at the second configuration (Fig. 12), where no interaction was found at the lateral arrangement, indicating that no chemical bonding would be seen in the experiment with this geometrical configuration. This tendency is also consistent with previous results,[65] where an intermolecular interaction with molecular systems has only been reported at the SWCNH tip.

According to the latter calculations, extended porphyrin **1** is not a good candidate for use in nanohybrid materials. Nevertheless, once the species is metalated with Au or Cu atoms, a dramatic change is observed, as electronic communication at a distance of 350 pm and 425 pm for the $Au_2$ and $Cu_2$ HPs, respectively, was found. The construction of nanohybrid materials with Au and Cu metalated extended porphyrins and SWCNHs may represent excellent candidates to be used as building blocks in solar cell materials, due to the facile electron communication among the species.

The experimentally observed absorption bands clearly indicate the absorption of energy in the visible region, which activates the electronic population on the HP; it may consequently be transferred to structures such as the SWCNHs reported in this work.
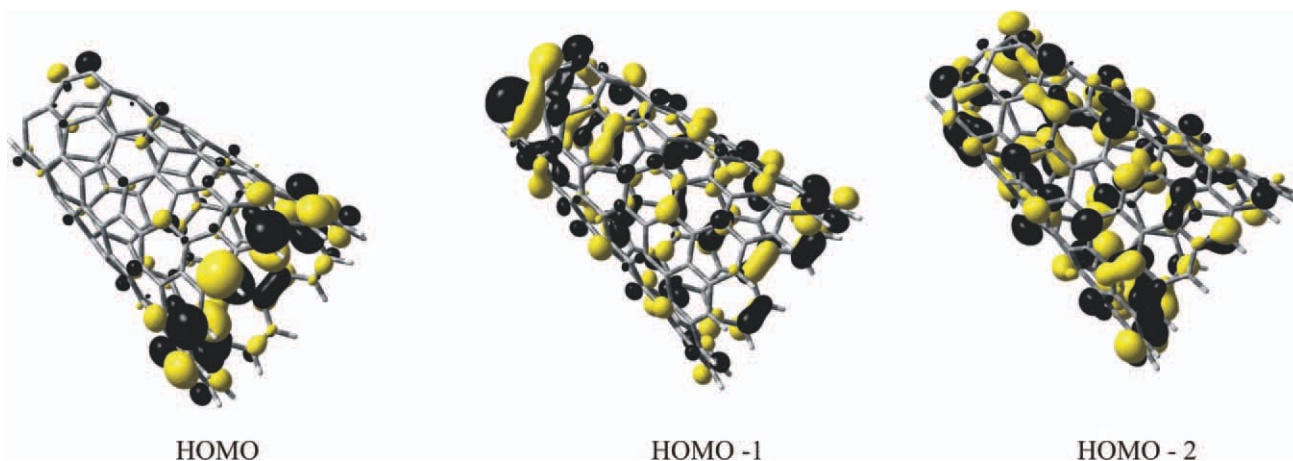


**Figure 13.** Spatial representation of the occupied frontier MOs of the 114-C atom SWCNH model system. [Color figure can be viewed in the online issue, which is available at wileyonlinelibrary.com.]

This analysis clearly reveals an electrostatic interaction (dipole or higher order attraction) among the HP species and the SWCNH. A further analysis to this statement may be verified from the orbital energies of the HP and SWCNH. Considering the $Au_2$ aromatic HP (Fig. 1c), its LUMO energy is $-0.1666$ hartrees, which is comparable to the SWCNH HOMO energy of $-0.1487$ hartrees, addressing the availability of electronic intercommunication in the nanohybrid compound.

On the other hand, the $Au_2$ antiaromatic compound **5** presents a LUMO energy of $-0.1469$ hartrees, which is basically the same than that of the SWCNH HOMO. This explains the stronger interaction found in this case, and it also explains the shortening of the equilibrium distance with regard to the aromatic analogue. The shift from aromatic to antiaromatic character after protonation of compound **3** stabilizes the orbital energy and consequently represents a good candidate for photovoltaic applications. This behavior is also observed in the $Cu_2$ species, where the HOMO is located at $-0.1647$ hartrees. In this case, a longer equilibrium distance of $\sim 400$ nm is reported (Fig. 11). This may be due to the large energy difference between the LUMO of the $Cu_2$ HP and the SWCNH HOMO energy (10 kcal/mol).

Compound **1**, with no metal attached to it, has a fully repulsive interaction. It can be explained from the spatial distribution of the LUMO, as seen in Figure 1a, where no contribution is found at the center of the ring. That contribution strictly appears when the metalation takes place. The LUMO contribution at the center of the ring gives a favorable region for electronic interaction with the SWCNHs. In particular, as has been shown, the face-to-face configuration is the most favorable geometrical arrangement to achieve a chemical interaction in the three cases presented in this work. This may be due to the spatial distribution of the highest occupied MOs at the SWCNHs, that is, the HOMO has no electronic population at the top of the structures, as depicted in Figure 13, but the HOMO-1 and HOMO-2 are particularly populated at the top of the structure, increasing the probability of interaction with the set of HPs.

## Conclusions

The nature of the aromatic and antiaromatic behavior of a group of metalated HPs has been studied. The geometrical structure of such systems is intimately related to the magnitude of the NICS values that dictate the strength of the aromaticity. The $\delta$-bonding present on the cycle of the metalated HP also plays a role in the aromatic character and rules the intrametallic character in the one-electron transitions involved in the excited states that give rise to the experimentally observed absorption bands. It is proposed that this group of systems may aid in building a nanohybrid material composed of a metalated HP and a SWCNH. The best site to induce an intermolecular interaction would be where the HP meets the SWCNH at its tip. In this way, proof of an intermolecular attraction was found and electronic communication between both species would be expected. This property is associated with materials that may be used as building blocks on photovoltaic

cells due to electronic transport. These results may motivate further syntheses and detailed experimental studies of such nanohybrid systems.

[1] J. L. Sessler, D. Seidel, *Angew. Chem. Int. Ed.* **2003**, *42*, 5134.

[2] Z. S. Yoon, A. Osuka, D. Kim, *Nat. Chem.* **2009**, *1*, 113.

[3] J. Y. Shin, K. S. Kim, M. C. Yoon, J. M. Lim, Z. S. Yoon, A. Osuka, D. Kim, *Chem. Soc. Rev.* **2010**, *39*, 2751.

[4] J. M. Lim, Z. S. Yoon, J. Y. Shin, K. S. Kim, M. C. Yoon, D. Kim, *Chem. Commun.* **2009**, *45*, 261.

[5] M. Pawlicki, H. A. Collins, R. G. Denning, H. L. Anderson, *Angew. Chem. Int. Ed.* **2009**, *48*, 3244.

[6] J. L. Sessler, E. Tomat, *Acc. Chem. Res.* **2007**, *40*, 371.

[7] R. Sakamoto, S. Saito, S. Shimizu, Y. Inokuma, N. Aratani, A. Osuka, *Chem. Lett.* **2010**, *39*, 439.

[8] M. Suzuki, M. C. Yoon, D. Y. Kim, J. H. Kwon, H. Furuta, D. Kim, A. Osuka, *Chem. Eur. J.* **2006**, *12*, 1754.

[9] S. Mori, S. Shimizu, R. Taniguchi, A. Osuka, *Inorg. Chem.* **2005**, *44*, 4127.

[10] S. Mori, A. Osuka, *J. Am. Chem. Soc.* **2005**, *127*, 8030.

[11] M. Toganoh, H. Furuta, *J. Org. Chem.* **2010**, *75*, 8213.

[12] S. Iijima, M. Yudasaka, R. Y. S. Bandow, K. Suenaga, F. Kokai, K. Takahashi, *Chem. Phys. Lett.* **1999**, *309*, 165.

[13] J. A. Nisha, M. Yudasaka, S. Bandow, F. Kokai, K. Takahashi, S. Iijima, *Chem. Phys. Lett.* **2000**, *328*, 381.

[14] K. Murata, K. Kaneko, H. Kanoh, D. Kasuya, K. Takahashi, F. Kokai, M. Yudasaka, S. Iijima, *J. Phys. Chem. B* **2002**, *106*, 11132.

[15] H. Tanaka, H. Kanoh, M. E. Merraoui, W. A. S. M. Yudasaka, S. Iijima, K. Kaneko, *J. Phys. Chem. B* **2004**, *108*, 17457.

[16] H. Murakami, K. Ajima, J. Miyawaki, M. Yudasaka, S. Iijima, K. Shiba, *Mol. Pharm.* **2004**, *1*, 399.

[17] E. Bekyarova, K. Murata, M. Y. D. Kasuya, S. Iijima, H. Tanaka, H. Kahoh, K. Kaneko, *J. Phys. Chem. B* **2003**, *107*, 4681.

[18] K. Murata, A. Hashimoto, M. Yudasaka, D. Kasuya, K. Kaneko, S. Iijima, *Adv. Mater.* **2004**, *16*, 1520.

[19] S. Zhu, G. Xu, *Nanoscale* **2010**, *2*, 2538.

[20] S. Zhu, L. Fan, X. Liu, L. Shi, H. Li, S. Han, G. Xu, *Electrochem. Commun.* **2008**, *10*, 695.

[21] S. Zhu, Z. Liu, W. Zhang, S. Han, L. Hu, G. Xu, *Chem. Commun.* **2011**, *47*, 6099.

[22] D. V. Kolesnikov, V. A. Osipov, *JETP Lett.* **2004**, *79*, 532.

[23] A. D. Becke, *J. Chem. Phys.* **1993**, *98*, 5648.

[24] M. J. S. Dewar, E. G. Zoebisch, E. F. Healy, J. J. P. Stewart, *J. Am. Chem. Soc.* **1985**, *107*, 3902.

[25] C. W. Bauschlicher, *Chem. Phys. Lett.* **2000**, *322*, 237.

[26] G. E. Froudakis, *Nano. Lett.* **2001**, *1*, 179.

[27] X. Lu, F. Tian, N. Wang, Q. Zhang, *J. Am. Chem. Soc.* **2003**, *125*, 10459.

[28] I. D. Petsalakis, G. Pagona, G. Theodorakopoulos, N. Tagmatarchis, M. Yudasaka, S. Iijima, *Chem. Phys. Lett.* **2006**, *429*, 194.

[29] P. Khongpracha, M. Probst, J. Limtrakul, *Eur. Phys. J. D* **2008**, *48*, 211.

[30] G. Pagona, A. S. D. Sandanayaka, Y. Araki, J. Fan, N. Tagmatarchis, G. Charalambidis, A. G. Coutsolelos, B. Boitrel, M. Yudasaka, S. Iijima, O. Ito, *Adv. Funct. Mater.* **2007**, *17*, 1705.

[31] H. Imahori, H. Iijima, T. U. Y. Hayashi Toude Matano, S. Ito, *Chem Sus Chem.* **2011**, *4*, 797.

[32] M. Z. Jacobson, M. A. Delucchi, *Sci. Am.* **2009**, *301*, 58.

[33] D. Wohrle, D. Meissner, *Adv. Mater.* **1991**, *3*, 129.

[34] N. S. Lewis, *Science* **2007**, *315*, 798.

[35] S. S. Sun, Organic Photovoltaics: Mechanisms, Materials, and Devices; CRC Press: Boca Raton, FL, **2005**.

[36] C. J. Brabec, V. Dyakonov, J. Parisi, N. S. Sariciftci, Organic Photovoltaics: Concepts and Realization; Springer: Berlin, **2010**.

[37] N. Beaumont, I. Hancox, P. Sullivan, R. A. Hatton, T. S. Jones, *Energy Environ. Sci.* **2011**, *4*, 1708.

[38] M. Riede, T. Mueller, W. Tress, R. Schueppel, K. Leo, *Nanotechnology* **2008**, *19*, 424001.

[39] C. W. Tang, *Appl. Phys. Lett.* **1986**, *48*, 183.

[40] K. Kalyanasundaram, Dye-Sensitized Solar Cells; CRC Press: Boca Raton, FL, **2010**.

[41] M. Pagliaro, G. Palmisano, R. Ciriminna, Flexible Solar Cells; Wiley-VCH: Weinheim, Germany, **2008**.

[42] M. A. Green, *Physica E* **2002**, *14*, 65.

[43] F. C. Krebs, Polymer Photovoltaics: A Practical Approach; SPIE Publications: Bellingham, WA, **2008**.

[44] M. Pagliaro, R. Ciriminna, G. Palmisano, *ChemSusChem.* **2008**, *1*, 880.

[45] S. R. Forrest, *Nature* **2004**, *428*, 911.

[46] D. Andrae, U. Haeussermann, M. Dolg, H. Stoll, H. Preuss, *Theor. Chim. Acta.* **1990**, *77*, 123.

[47] A. Schäfer, C. Huber, R. Ahlrichs, *J. Chem. Phys.* **1994**, *100*, 5829.

[48] G. A. Petersson, M. A. Al-Laham, *J. Chem. Phys.* **1991**, *94*, 6081.

[49] G. A. Petersson, A. Bennett, T. G. Tensfeldt, M. A. Al-Laham, W. A. Shirley, J. Mantzaris, *J. Chem. Phys.* **1988**, *89*, 2193.

[50] S. F. Boys, F. Bernardi, *Mol. Phys.* **1970**, *19*, 553.

[51] S. Grimme, *J. Comput. Chem.* **2006**, *27*, 1787.

[52] A. D. Becke, *J. Chem. Phys.* **1997**, *107*, 8554.

[53] M. E. Casida, C. Jamorski, K. C. Casida, D. R. Salahub, *J. Chem. Phys.* **1998**, *108*, 4439.

[54] Y. Zhao, D. Truhlar, *J. Phys. Chem. A* **2006**, *110*, 13126.

[55] A. Dreuw, M. Head-Gordon, *J. Am. Chem. Soc.* **2004**, *126*, 4007.

[56] J. Tomasi, B. Mennucci, R. Cammi, *Chem. Rev.* **2005**, *105*, 2999.

[57] E. D. Glendening, A. E. Reed, J. E. Carpenter, F. Weinhold, NBO version 3.1.

[58] P. v. R. Schleyer, C. Maerker, A. Dransfeld, H. v. E. Jiao, N. J. Hommes, *J. Am. Chem. Soc.* **1996**, *118*, 6317.

[59] M. J. Frisch, G. W. Trucks, H. B. Schlegel, G. E. Scuseria, M. A. Robb, J. R. Cheeseman, G. Scalmani, V. Barone, B. Mennucci, G. A. Petersson, H. Nakatsuji, M. Caricato, X. Li, H. P. Hratchian, A. F. Izmaylov, J. Bloino, G. Zheng, J. L. Sonnenberg, M. Hada, M. Ehara, K. Toyota, R. Fukuda, J. Hasegawa, M. Ishida, T. Nakajima, Y. Honda, O. Kitao, H. Nakai, T. Vreven, J. A. Montgomery, Jr., J. E. Peralta, F. Ogliaro, M. Bearpark, J. J. Heyd, E. Brothers, K. N. Kudin, V. N. Staroverov, R. Kobayashi, J. Normand, K. Raghavachari, A. Rendell, J. C. Burant, S. S. Iyengar, J. Tomasi, M. Cossi, N. Rega, J. M. Millam, M. Klene, J. E. Knox, J. B. Cross, V. Bakken, C. Adamo, J. Jaramillo, R. Gomperts, R. E. Stratmann, O. Yazyev, A. J. Austin, R. Cammi, C. Pomelli, J. W. Ochterski, R. L. Martin, K. Morokuma, V. G. Zakrzewski, G. A. Voth, P. Salvador, J. J. Dannenberg, S. Dapprich, A. D. Daniels, Ö. Farkas, J. B. Foresman, J. V. Ortiz, J. Cioslowski, D. J. Fox, Gaussian 09 Revision A.1; Gaussian Inc.: Wallingford, CT, **2009**.

[60] J. Muñiz, L. E. Sansores, A. Martínez, R. Salcedo, *J. Mol. Model.* **2008**, *14*, 417.

[61] J. Muñiz, L. E. Sansores, P. Pyykko, A. Martínez, R. Salcedo, *J. Mol. Model.* **2009**, *15*, 1165.

[62] C. S. Wannere, C. Corminboeuf, Z. X. Wang, M. D. Wodrich, R. B. v. R. King, P. Schleyer, *J. Am. Chem. Soc.* **2005**, *127*, 5701.

[63] B. Champagne, E. A. Perpete, S. J. A. van Gisbergen, E. J. Baerends, J. G. S. C. A. K. Soubra-Ghaoui, K. A. Robins, B. Kirtman, *J. Chem. Phys.* **1998**, *109*, 10489.

[64] Y. Zhao, D. G. Truhlar, *J. Phys. Chem. A* **2006**, *110*, 10478.

[65] I. D. Petsalakis, G. Pagona, N. Tagmatarchis, G. Theodorakopoulos, *Chem. Phys. Lett.* **2007**, *448*, 115.